

Current-induced spin polarization in spin-orbit-coupled two-dimensional electron systems

Ming-Hao Liu, Son-Hsien Chen, and Ching-Ray Chang
 Department of Physics, National Taiwan University, Taipei 10617, Taiwan
 (Dated: March 12, 2019)

Current-induced spin polarization (CISP) is rederived in ballistic spin-orbit-coupled two-dimensional electron systems, based on the equilibrium statistical mechanics. A simple and useful picture is correspondingly proposed to help understand the CISP and predict the polarization direction. Nonequilibrium Landauer-Keldysh formalism is applied to demonstrate the validity of the statistical picture. Spin densities induced by the CISP in semiconductor heterostructures and in metallic surface states are compared, showing that the CISP increases with the spin-splitting strength and hence suggesting that the CISP should be more observable on metal/semimetal surfaces due to the discovered strong Rashba splitting. An application of the CISP designed to generate a spin-Hall pattern in the inplane, instead of the out-of-plane, component is also proposed.

PACS numbers: 72.25.Pn, 71.70.Ej, 85.75.-d

I. INTRODUCTION

The aim of preparing and controlling spins in all-electrical nonmagnetic devices has been shown to be possible in semiconducting bulk and two-dimensional electron systems (2DESs).^{1,2} Besides the optical spin injection, a much more natural way of spin orientation is to make use of the spin-orbit (SO) coupling due to the lack of inversion symmetry of the underlying material.³ When passing an unpolarized electric current (electrons carrying random spins) through an SO-coupled material, spin-dependent consequences arise, among which two famous phenomena are the spin-Hall effect (SHE)^{4,5,6,7,8,9} and the current-induced spin polarization (CISP).

In the CISP phenomenon, unpolarized electric current is expected to be spin-polarized when flowing in a SO-coupled sample. This effect was first theoretically proposed in the early 90s. Edelstein employed linear-response theory to calculate the spin polarization due to an electric current in the presence of SO coupling linear in momentum, taking into account low-concentration impurities.¹⁰ Aronov *et al.* solved the quantum Liouville's theorem for the spin density matrix to show the CISP,¹¹ taking into account scattering as well. Recently, the CISP phenomenon has been experimentally proved.^{12,13,14} Moreover, both the SHE and CISP have been observed at room temperature.¹⁵

In this paper we propose another viewpoint based on equilibrium statistical mechanics to explain the CISP induced by SO coupling linear in momentum in ballistic 2DESs, i.e., without impurity scattering. We show that the canonical ensemble average (CEA) of electron spins moving with a wave vector \mathbf{k} immediately prescribes a spin polarization antiparallel to the effective magnetic field $\mathbf{B}_{\text{eff}}(\mathbf{k})$ induced by the underlying SO coupling, and hence explains the CISP. Correspondingly, a much simpler picture, compared to the early theoretical works Refs. 10 and 11, helps provide a qualitative and straightforward explanation for the CISP: In an SO cou-

pled 2DES without external magnetic field, an ensemble of rest electrons is unpolarized, while it becomes spin-polarized antiparallel to $\mathbf{B}_{\text{eff}}(\mathbf{k})$ when moving along \mathbf{k} [see Fig. 1(a)].

To demonstrate the validness of this elementary statistical argument, spin and charge transport in finite-size four-terminal conducting 2DESs [see Fig. 1(b)] will be numerically analyzed using the more sophisticated Landauer-Keldysh formalism (LKF),^{16,17} allowing for nonequilibrium statistics. Good agreement between the analytical CEA and the numerical LKF will be seen, consolidating our statistical picture. An application of the CISP, resembling an inplane SHE, will be subsequently proposed. Finally, we extend the analysis of the CISP to different materials including semiconducting heterostructures and metal/semimetal surfaces, and compare the polarization strengths. Throughout this paper, all the band parameters used in the LKF are extracted from experiments by matching the band structures calculated by the tight-binding model (and hence the density of states calculated by the LKF) with the experimentally measured ones.¹⁸

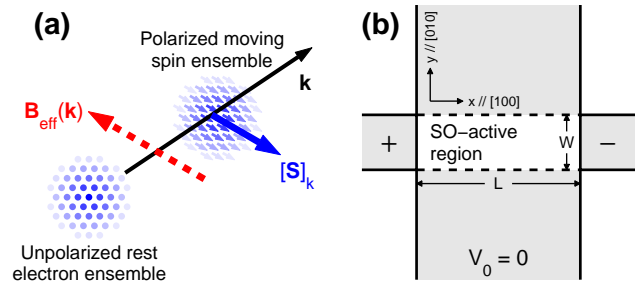


FIG. 1: (Color online) (a) Statistical picture of the current-induced spin polarization phenomenon. (b) Schematic of a four-terminal setup to be analyzed by employing the Landauer-Keldysh formalism. The left and right leads are biased to drive the electrons moving forward. Unbiased top and bottom leads are for suppressing the boundary effect.

II. ANALYTICAL FORMULA: CANONICAL ENSEMBLE AVERAGE

We begin by deriving the analytical CEA expression of electron spins in an SO-coupled 2DES. In quantum statistics, any physical quantity, say A , is expressed in terms of the quantum statistical average $[A] = \text{Tr}(\rho A)$. Adopting the canonical ensemble, the average reads

$$[A] = \frac{\text{Tr} \left(e^{-\mathcal{H}/k_B T} A \right)}{\sum_\nu e^{-E_\nu/k_B T}}, \quad (1)$$

where k_B is the Boltzmann constant, T is temperature, ν is a quantum number labeling the states, and E_ν is the eigenenergy of state ν solved from Hamiltonian \mathcal{H} . Now consider an unpolarized electron ensemble in a 2DES, subject to

$$\mathcal{H} = \frac{\mathbf{p}^2}{2m} + \mathbf{S} \cdot \vec{\Omega}(\mathbf{p}), \quad (2)$$

with the effective mass m , the spin operator $\mathbf{S} = (\hbar/2)\vec{\sigma}$, $\vec{\sigma} \equiv (\sigma^x, \sigma^y, \sigma^z)$ being the Pauli matrix vector, and the momentum-dependent Larmor frequency $\vec{\Omega}(\mathbf{p}) = (e/mc)\mathbf{B}_{\text{eff}}(\mathbf{p})$, $\mathbf{B}_{\text{eff}}(\mathbf{p})$ being the effective magnetic field induced by the SO coupling.¹⁹ For the linear Rashba model,^{3,19,20} the Larmor frequency is of the form $\vec{\Omega}_R = (2\alpha/\hbar^2)\mathbf{p} \times \hat{n}$ with \hat{n} the unit vector along the norm of the 2DES, while for the linear Dresselhaus [001] model,^{3,19,21} we have $\vec{\Omega}_D^{[001]} = (2\beta/\hbar^2)(p_x, -p_y, 0)$. Here α and β are commonly referred to as the Rashba and Dresselhaus SO coupling strengths, respectively. Diagonalization of Eq. (2), in principle, gives a pair ($2 \times \frac{1}{2} + 1 = 2$) of momentum-dependent eigenspinors $|\sigma, \mathbf{k}\rangle$, satisfying $\mathcal{H}|\sigma, \mathbf{k}\rangle = E_\sigma(\mathbf{k})|\sigma, \mathbf{k}\rangle$ with $E_\sigma(\mathbf{k}) = \hbar^2 k^2/2m + \sigma\Delta_{\mathbf{k}}$, $\sigma = \pm 1$. In the Rashba-Dresselhaus [001] linear model, the zero-field spin-splitting reads $\Delta_{\mathbf{k}} = \zeta_{\mathbf{k}}k$ with $\zeta_{\mathbf{k}} = \sqrt{\alpha^2 + \beta^2 + 2\alpha\beta \sin 2\phi_{\mathbf{k}}}$, where $\phi_{\mathbf{k}}$ is the angle of $\mathbf{k} = (k_x, k_y)$ relative to [100] (Refs. 3,22).

Of our main interest here is the CEA of the spin operators of an ensemble of electrons, subject to an identical wave vector \mathbf{k} . By this we mean that the summation in Eq. (1) runs over the spin index σ only. This gives $[\mathbf{S}]_{\mathbf{k}} = (\hbar/2) \text{Tr}(e^{-\mathcal{H}/k_B T} \vec{\sigma}) / \sum_{\sigma=\pm} e^{-E_\sigma(\mathbf{k})/k_B T}$. Choosing the basis $|\sigma, \mathbf{k}\rangle$ for the trace, one is led to $[\mathbf{S}]_{\mathbf{k}} = (\hbar/2) [\sum_\sigma e^{-E_\sigma(\mathbf{k})/k_B T} \langle \sigma, \mathbf{k} | \vec{\sigma} | \sigma, \mathbf{k} \rangle] / \sum_\sigma e^{-E_\sigma(\mathbf{k})/k_B T}$. Noting $\langle -\sigma, \mathbf{k} | \vec{\sigma} | -\sigma, \mathbf{k} \rangle = -\langle \sigma, \mathbf{k} | \vec{\sigma} | \sigma, \mathbf{k} \rangle$ ²³ and factoring out $e^{-\hbar^2 k^2/2mk_B T}$ from $e^{-E_\sigma/k_B T}$, we arrive at the general expression

$$[\mathbf{S}]_{\mathbf{k}} = -\frac{\hbar}{2} \tanh \frac{\Delta_{\mathbf{k}}}{k_B T} \langle \sigma, \mathbf{k} | \vec{\sigma} | \sigma, \mathbf{k} \rangle, \quad (3)$$

where $\langle +1, \mathbf{k} | \vec{\sigma} | +1, \mathbf{k} \rangle$ corresponds to the effective magnetic field direction $\mathbf{B}_{\text{eff}}(\mathbf{k})/|\mathbf{B}_{\text{eff}}(\mathbf{k})|$. Therefore, Eq. (3) predicts that in an SO coupled 2DES, an ensemble of rest electrons ($\mathbf{k} \rightarrow 0$) is unpolarized ($[\mathbf{S}]_{\mathbf{k} \rightarrow 0} =$

$0 \because \Delta_{\mathbf{k} \rightarrow 0} = 0$) and becomes spin-polarized antiparallel to $\mathbf{B}_{\text{eff}}(\mathbf{k})$ when moving with \mathbf{k} , as schematically shown in Fig. 1(a). Moreover, the hyperbolic tangent factor $\tanh(\Delta_{\mathbf{k}}/k_B T)$ clearly predicts the decrease with T and the increase with $\Delta_{\mathbf{k}}$ in the polarization magnitude, and therefore explains two signatures of the CISP qualitatively: (i) The CISP can persist up to the room temperature. Taking $\Delta_{\mathbf{k}} \approx 3.68$ meV from Ref. 14 one has $\tanh[\Delta_{\mathbf{k}}/(k_B \times 300 \text{ K})] / \tanh[\Delta_{\mathbf{k}}/(k_B \times 10 \text{ K})] \approx 14\%$. (ii) As $\langle \mathbf{k} \rangle \propto V_0$ (Ref. 13) implies $\Delta_{\mathbf{k}} \propto V_0$, the magnitude of the CISP governed by $\tanh(\Delta_{\mathbf{k}}/k_B T)$ is supposed to increase with the bias, as is experimentally proved.¹²

Taking the Rashba-Dresselhaus [001] linear model for example, in which the effective magnetic field direction is given by $\langle \sigma, \mathbf{k} | \vec{\sigma} | \sigma, \mathbf{k} \rangle = (\sin \varphi_{\mathbf{k}}, -\cos \varphi_{\mathbf{k}}, 0)$ with $\varphi_{\mathbf{k}} \equiv \arg[(\alpha \cos \phi_{\mathbf{k}} + \beta \sin \phi_{\mathbf{k}}) + i(\alpha \sin \phi_{\mathbf{k}} + \beta \cos \phi_{\mathbf{k}})]$ (Ref. 22), Eq. (3) gives

$$[\mathbf{S}]_{\mathbf{k}} = -\frac{\hbar}{2} \tanh \frac{\zeta_{\mathbf{k}} k}{k_B T} (\sin \varphi_{\mathbf{k}}, -\cos \varphi_{\mathbf{k}}, 0). \quad (4)$$

III. NUMERICAL RESULTS: LANDAUER-KELDysh FORMALISM

To inspect the validity of the previously proposed statistical picture and further examine the CISP, we now perform local spin density calculation in finite-size 2DESs attached to four normal metal leads by using the LKF.^{16,17} Throughout this section except Sec. III E, we will concentrate on the $\mathbf{k} \parallel \hat{x}$ transport by applying potential difference V_0 between the left and right leads, and switch on unbiased ($V_0 = 0$) top and bottom leads to suppress the boundary effect, as shown in Fig. 1(b).

A. Local spin densities in extreme Rashba and Dresselhaus [001] cases

As a preliminary demonstration, Fig. 2 shows the position-dependent inplane spin vectors $\langle \mathbf{S} \rangle_{\mathbf{r}}^{\parallel} = (\langle S_x \rangle_{\mathbf{r}}, \langle S_y \rangle_{\mathbf{r}})$, with the local spin densities $\langle S_x \rangle_{\mathbf{r}}$ and $\langle S_y \rangle_{\mathbf{r}}$ calculated by the LKF. Here we adopt the finite difference method and discretize the $30a \times 10a$ channel, made of InGaAs/InAlAs heterostructure²⁴ along [001], into a square lattice with lattice spacing $a = 1$ nm. Accordingly, this gives the kinetic and Rashba hopping strengths $t_0 \equiv \hbar^2/2m^*a^2 = 0.762$ eV and $t_R \equiv \alpha/2a = 3.6$ meV, respectively. For the Dresselhaus hopping strength, we set $t_D \equiv \beta/2a = 1.33$ meV with $\beta \approx \gamma \langle k_z^2 \rangle$ and $\gamma \approx 27$ eV \AA^3 for GaAs and InAs.³

Let us first consider the extreme cases, pure Rashba and pure Dresselhaus [001] channels. As expected, the spin vectors are mostly oriented antiparallel to $\mathbf{B}_{\text{eff}}(\mathbf{k})$, which is, for $\mathbf{k} \parallel \hat{x}$, pointing to $-\hat{y}$ in the Rashba channel [Fig. 2(a)/(c) with low/high bias], and $+\hat{x}$ in the Dresselhaus [001] channel [Figs. 2(b)/(d) with low/high

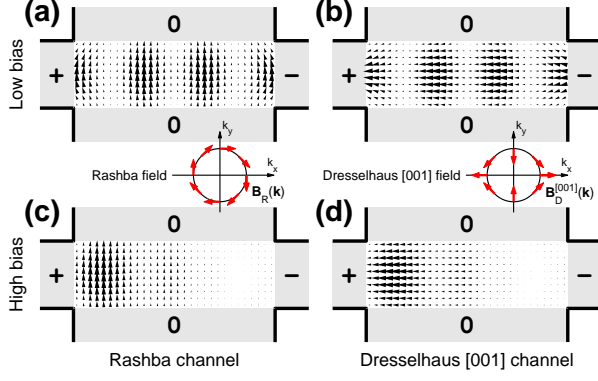


FIG. 2: (Color online) Spin orientation in a $30a \times 10a$ channel with $a = 1$ nm. Channels with linear Rashba model are considered in (a) and (c) while those with linear Dresselhaus [001] model are in (b) and (d). The direction of each sharp triangle represents the inplane spin vector $\langle \mathbf{S} \rangle_{\parallel} = (\langle S_x \rangle, \langle S_y \rangle)$ of the local spin density. The size of the triangle depicts the magnitude of $\langle \mathbf{S} \rangle_{\parallel}$. Effective magnetic fields due to individually the Rashba and the Dresselhaus [001] fields are shown in the insets.

bias]. Here (and hereafter) the low and high biases mean $eV_0 = 2$ meV and 0.2 eV, respectively, and we label the applied potential energy of $\pm eV_0/2$ as “ \pm ” and $eV_0 = 0$ as “0” on each lead. Note that the spin distribution, modulated by the charge distribution, forms standing waves in the low bias regime since the electrons behaves quantum mechanically, while that in the high bias regime, i.e., the nonequilibrium transport regime, decays with distance.¹⁸ The polarization in the latter (high bias) is about two order of magnitude stronger than the former (low bias).

B. Consistency check: Analytical CEA vs. numerical LKF

We now examine a set of $30a \times W$ channels, all with nonvanishing t_R and t_D , and focus on the quantity $S_{xy} \equiv [S_x]/[S_y]$. Since we are considering $\phi_{\mathbf{k}} = 0$, from the CEA formula Eq. (4) with $\phi_{\mathbf{k}=(k,0)} = \arg(\alpha + i\beta) = \tan^{-1}(\beta/\alpha)$ ($\alpha > 0, \beta > 0$) gives $S_{xy}^{\text{CEA}} = ([S_x]/[S_y])_{\mathbf{k}=(k,0)} = -\tan \phi_{\mathbf{k}} = -\beta/\alpha = -t_D/t_R$. On the other hand, in averaging $\langle S_x \rangle_{\mathbf{r}}$ and $\langle S_y \rangle_{\mathbf{r}}$, computed by the LKF, of all the lattice points \mathbf{r} within the conducting channel, we define $S_{xy}^{\text{LKF}} \equiv \sum_{\mathbf{r}} \langle S_x \rangle_{\mathbf{r}} / \sum_{\mathbf{r}} \langle S_y \rangle_{\mathbf{r}}$. In the following we compare S_{xy}^{LKF} with S_{xy}^{CEA} and calculate the deviation $\Delta S_{xy} \equiv (S_{xy}^{\text{LKF}} - S_{xy}^{\text{CEA}}) / |S_{xy}^{\text{CEA}}|$ to show the consistency between the analytical CEA formula and the numerical LKF results.

Let us first consider channel widths $W_1 = 10a$, $W_2 = 20a$, and $W_3 = 30a$, and tune the Rashba coupling within an experimentally reasonable range.²⁴ The Dresselhaus coupling is fixed at $t_D = 1.33$ meV [same as Fig. 2(b)].

As shown in Figs. 3(a) and (b) with low and high biases, respectively, ΔS_{xy} for both bias regimes and for all the three channel widths are within only a few percents. Tiny differences among these six curves indicate that the CEA argument works better in the high bias regime and in narrower channels. The argument becomes even exact when $t_R = t_D$ meets, under which interesting physics occurs.^{25,26}

Next we take a further look at ΔS_{xy} for its channel width dependence in both bias regimes. We change W from W_1 to W_3 and fix t_R and t_D at those put in Figs. 2(a) and 2(b), respectively. As shown in Fig. 3(c), the general trend for both bias regimes agrees with the previous observation that ΔS_{xy} is lower for narrower W , except the additional oscillation behavior of the low-bias curve. As discussed recently in Ref. 18, the spin accumulation pattern is sensitive to Fermi level E_F in the low bias regime (in which electrons are well described by wave functions) due to the change of the Fermi wavelength λ_F . Likewise, fixing E_F but varying the sample size as well influences the wave function and hence the charge distribution, which modifies the spin accumulation pattern, including the inplane components $\langle \mathbf{S} \rangle_{\parallel}$. On the other hand, equilibrium picture does not hold in the high bias regime so that $\langle \mathbf{S} \rangle_{\parallel}$ is less affected by the varying of W . These explain the sensitivity/insensitivity of the low/high bias curve in Fig. 3(c).

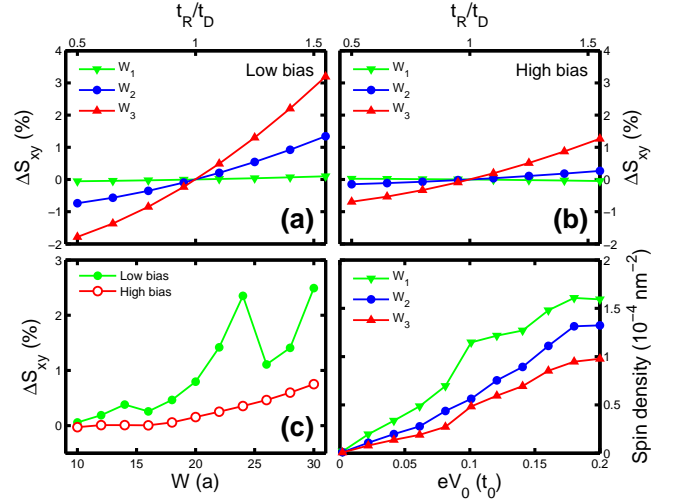


FIG. 3: (Color online) Deviation between the CEA and the LKF results ΔS_{xy} as a function of the Rashba hopping strength with (a) low bias and (b) high bias, considering $W_1 = 10a$, $W_2 = 20a$, and $W_3 = 30a$. (c) shows the width dependence of ΔS_{xy} for both the low and high bias. In (d) the bias dependence of spin densities induced by the CISP is shown, considering Rashba channels.

C. Bias Dependence of CISP

Having shown that the statistical argument indeed works well, we next examine the bias dependence of the CISP, which is expected to be a proportional relation, as has been experimentally observed.¹² We return to Rashba channels. Spin densities, i.e., the total spin divided by the total area of the conducting channel, obtained via $\sum_{\mathbf{r}} \langle S_y \rangle_{\mathbf{r}} / (Na^2)$ here with N being the number of total lattice sites in the conducting sample, are reported in Fig. 3(d) for $W = W_1, W_2, W_3$. Consistent to the experiment, the calculated spin densities increase with eV_0 . In addition, linear response within $eV_0 \lesssim 0.1t_0 = 0.076$ eV is clearly observed in all cases. Nonlinearity enters when eV_0 grows so that nonequilibrium statistics dominates. Note that the calculated local spin density distribution satisfies the usual SHE symmetry,¹⁷ so that we have $\sum_{\mathbf{r}} \langle S_x \rangle_{\mathbf{r}} = \sum_{\mathbf{r}} \langle S_z \rangle_{\mathbf{r}} = 0$ and $|\sum_{\mathbf{r}} \langle \mathbf{S} \rangle_{\mathbf{r}}| = \sum_{\mathbf{r}} \langle S_y \rangle_{\mathbf{r}}$.

D. Comparison of CISP in semiconductor heterostructures and metal/semimetal surface states

Next we extend the calculation of the spin density due to the CISP to other materials. In addition to semiconductor heterostructures, 2DESs have been shown to exist also on metal surfaces supported by the surface states.²⁷ Due to the loss of inversion symmetry, the metallic surfaces may exhibit Rashba spin-splitting as well.²⁸ Here we consider three samples: 54×18 nm² InGaAs/InAlAs heterostructure, 14.7×4.9 nm² Au(111) surface, and 16.2×5.4 nm² Bi(111) surface. For all of the three samples we arrange the lead configuration as that in Fig. 1(b) and apply high bias. The sizes we choose here are to maintain the same lattice site number $N \lesssim 1000$ and keep the length-width ratio ~ 3 . Note that realistic lattice structure are considered for the surface states [triangular for Au(111) and honeycomb for Bi(111) bilayer], while finite-difference method based on the long-wavelength limit for the heterostructure is adopted.

Band parameters extracted from experiments and the

Material	InGaAs/InAlAs (heterostructure)	Au(111) (surface state)	Bi(111) (surface state)
m/m_0	0.050	0.251	0.340
α (eV Å)	0.072	0.356	0.829
$E_F - E_b$ (eV)	0.108	0.417	0.083
Reference	24	29	30
CISP (10^{-3} nm ⁻²)	0.240	2.742	8.382

TABLE I: Summary of effective mass ratio m/m_0 , Rashba constant α , Fermi energy E_F (relative to the band bottom E_b), and the calculated spin density due to CISP, for a set of materials.

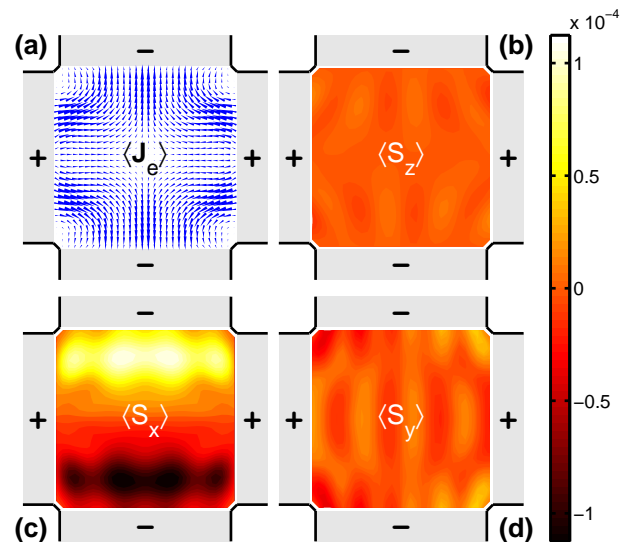


FIG. 4: (Color online) Mapping of the (a) local charge current density, local spin densities (b) $\langle S_z \rangle$, (c) $\langle S_x \rangle$, and (d) $\langle S_y \rangle$ in a four-terminal square channel with a special bias arrangement. Unit in (b)–(c) is $\hbar/2$.

spin densities calculated by the LKF are summarized in Table I. Clearly, the CISP increases with the Rashba parameter α . This suggests that the CISP (and actually also the SHE) should be observable on these surfaces. The recently discovered Bi/Ag(111) surface alloy which exhibits a giant spin splitting³¹ is even more promising, but we do not perform calculation for this interesting material here.

E. Application of CISP: Generation of Inplane Spin-Hall Pattern

Finally, we propose an experimental setup, as an application of the CISP, to generate an antisymmetric edge spin accumulation in the inplane component, i.e., an inplane spin-Hall pattern. The conducting sample is of the Rashba type and the parameters for the LKF calculation are taken the same as those in Fig. 3(d). Sample size is about 30×30 nm². We apply high bias of $eV_0 = 0.2$ eV and arrange a special bias configuration.

As shown in Fig. 4(a), unpolarized electron currents are injected from the left and right leads and are guided to the top and bottom ones. Under such design, the spin accumulation in $\langle S_z \rangle_{\mathbf{r}}$ exhibits merely a vague pattern [see Fig. 4(b)]. Contrarily, the pattern of $\langle S_x \rangle_{\mathbf{r}}$ shows not only antisymmetric edge accumulation in the channel but also stronger magnitude than the out-of-plane component [see Fig. 4(c)]. This pattern is reasonably expected by the CISP due to the opposite charge flows along $\pm \hat{y}$ at the top and bottom edges, and hence resembles an inplane SHE.

In determining $\langle S_y \rangle_r$, Fig. 4(d) does not show a rotated pattern from $\langle S_x \rangle_r$ due to the nonequilibrium transport. In the nonequilibrium transport regime, a distance apart from the source leads is required to induce the CISP, and therefore no significant $\langle S_y \rangle_r$ is observed near the source (left and right) leads. This can be seen by comparing the local spin density distributions in the low-bias and high-bias regimes shown in Fig. 2(a)/(b) and Figs. 2(c)/(d), respectively.

IV. SUMMARY

In conclusion, we have rederived the CISP phenomenon in the absence of impurity scattering based on equilibrium statistical mechanics. Correspondingly, a simple picture [Fig. 1(a)] is proposed to help qualitatively explain the CISP. The picture is further tested to work well even in the regime of nonequilibrium transport in finite-size samples, by employing the numeri-

cal LKF. Extending the spin density calculation from the semiconductor heterostructure to metal/semimetal surface states, our calculation confirms that the polarization increases with the Rashba coupling strength and hence suggests that the CISP should be more observable on metal/semimetal surfaces with stronger Rashba SO coupling.^{29,30,31} As an application of the CISP, we also suggest an interesting bias configuration for the 4-terminal setup to generate inplane SHE [Fig. 4(c)].

Acknowledgments

One of the authors (M.H.L.) appreciates S. D. Ganichev and L. E. Golub for valuable discussion, and L. Ding and G. Bihlmayer for useful information. Financial support of the Republic of China National Science Council Grant No. 95-2112-M-002-044-MY3 is gratefully acknowledged.

-
- ¹ *Semiconductor Spintronics and Quantum Computation*, edited by D. D. Awschalom, D. Loss, and N. Samarth (Springer, Berlin, 2002), chapters 4 and 5.
 - ² Y. Kato, R. C. Myers, A. C. Gossard, and D. D. Awschalom, *Nature (London)* **427**, 50 (2004).
 - ³ Roland Winkler, *Spin-Orbit Coupling Effects in Two-Dimensional Electron and Hole Systems* (Springer, Berlin, 2003).
 - ⁴ M. I. D'yakonov and V.I. Perel', *Zh. Eksp. Teor. Fiz.* **13**, 657 (1971) [*Sov. Phys. JEPT* **33**, 467 (1971)].
 - ⁵ J. E. Hirsch, *Phys. Rev. Lett.* **83**, 1834 (1999).
 - ⁶ S. Murakami, N. Nagaosa, and S. C. Zhang, *Science* **301**, 1348 (2003).
 - ⁷ J. Sinova, D. Culcer, Q. Niu, N.A. Sinitsyn, T. Jungwirth, and A.H. MacDonald, *Phys. Rev. Lett.* **92**, 126603 (2004).
 - ⁸ Y. K. Kato, R. C. Myers, A. C. Gossard, D. D. Awschalom, *Science* **306**, 1117 (2004).
 - ⁹ J. Wunderlich, B. Kaestner, J. Sinova, and T. Jungwirth, *Phys. Rev. Lett.* **94**, 047204 (2005).
 - ¹⁰ V. M. Edelstein, *Solid State Commun.* **73**, 233 (1990).
 - ¹¹ A. G. Aronov, Y. B. Lyanda-Geller, and G. E. Pikus, *Sov. Phys. JETP* **73**, 537 (1991).
 - ¹² Y. K. Kato, R. C. Myers, A. C. Gossard, and D. D. Awschalom, *Phys. Rev. Lett.* **93**, 176601 (2004).
 - ¹³ V. Shi, R. C. Myers, Y. K. Kato, W. H. Lau, A. C. Gossard, and D. D. Awschalom, *Nat. Phys.* **1**, 31 (2005).
 - ¹⁴ C. L. Yang, H. T. He, Lu Ding, L. J. Cui, Y. P. Zeng, J. N. Wang, and W. K. Ge, *Phys. Rev. Lett.* **96**, 186605 (2006).
 - ¹⁵ N. P. Stern, S. Ghosh, G. Xiang, M. Zhu, N. Samarth, and D. D. Awschalom, *Phys. Rev. Lett.* **97**, 126603 (2006).
 - ¹⁶ Branislav K. Nikolić, Satofumi Souma, Liviu P. Zârbo, and Jairo Sinova, *Phys. Rev. Lett.* **95**, 046601 (2005).
 - ¹⁷ Branislav K. Nikolić, Liviu P. Zârbo, and Satofumi Souma, *Phys. Rev. B* **73**, 075303 (2006).
 - ¹⁸ Ming-Hao Liu, Gustav Bihlmayer, Stefan Blügel, and Ching-Ray Chang, *Phys. Rev. B* **76**, 121301(R) (2007).
 - ¹⁹ I. Žutić, J. Fabian, and S. Das Sarma, *Rev. Mod. Phys.* **76**, 323 (2004), Sec. III B2.
 - ²⁰ Y. A. Bychkov and E. I. Rashba, *J. Phys. C* **17**, 6039 (1984).
 - ²¹ G. Dresselhaus, *Phys. Rev.* **100**, 580 (1955).
 - ²² Ming-Hao Liu, Kuo-Wei Chen, Son-Hsien Chen, and Ching-Ray Chang, *Phys. Rev. B* **74**, 235322 (2006).
 - ²³ Whereas we are concerning a group of electrons with an identical \mathbf{k} , one can regard the Larmor frequency as a constant vector $\vec{\Omega}(\mathbf{k})$, so that $\langle \sigma, \mathbf{k} | \vec{\sigma} \cdot \vec{\Omega}(\mathbf{k}) | \sigma, \mathbf{k} \rangle = \langle \sigma, \mathbf{k} | \vec{\sigma} | \sigma, \mathbf{k} \rangle \cdot \vec{\Omega}(\mathbf{k}) = \sigma \Delta_{\mathbf{k}}$ implies $\langle \pm, \mathbf{k} | \vec{\sigma} | \pm, \mathbf{k} \rangle = -\langle \mp, \mathbf{k} | \vec{\sigma} | \mp, \mathbf{k} \rangle$.
 - ²⁴ J. Nitta, T. Akazaki, H. Takayanagi, and T. Enoki, *Phys. Rev. Lett.* **78**, 1335 (1997).
 - ²⁵ J. Schliemann, J. C. Egues, and D. Loss, *Phys. Rev. Lett.* **90**, 146801 (2003).
 - ²⁶ B. A. Bernevig, J. Orenstein, and S.-C. Zhang, *Phys. Rev. Lett.* **97**, 236601 (2006).
 - ²⁷ W. Shockley, *Phys. Rev.* **56**, 317 (1939).
 - ²⁸ G. Bihlmayer, Yu. M. Koroteev, P. M. Echenique, E. V. Chulkov, and S. Blügel, *Surf. Sci.* **600**, 3888 (2006).
 - ²⁹ S. LaShell, B. A. McDougall, and E. Jensen, *Phys. Rev. Lett.* **77**, 3419 (1996).
 - ³⁰ Y. M. Koroteev, G. Bihlmayer, J. E. Gayone, E. V. Chulkov, S. Blügel, P. M. Echenique, and P. Hofmann, *Phys. Rev. Lett.* **93**, 046403 (2004).
 - ³¹ Cristian R. Ast, Jürgen Henk, Arthur Ernst, Luca Moreschini, Mihaela C. Falub, Daniela Pacilé, Patric Bruno, Klaus Kern, and Marco Grioni, *Phys. Rev. Lett.* **98**, 186807 (2007).